

Bosonic metal states in crystalline iron-based superconductors at the two-dimensional limit

Yanan Li^{1,5#}, Yi Liu^{2#}, Haiwen Liu³, Shichao Qi¹, Haoran Ji¹, Wenfeng Dong⁴, Yi Sun¹, Wenhao Zhang^{4,6}, Chengcheng Ji¹, Zihan Cui², Nitin Samarth⁵, Lili Wang⁴, X.C. Xie^{1,7,8}, Qi-Kun Xue^{4,8,9}, and Jian Wang^{1,7,8*}

¹*International Center for Quantum Materials, School of Physics, Peking University, Beijing 100871, China*

²*Department of Physics, Renmin University of China, Beijing 100872, China*

³*Center for Advanced Quantum Studies, Department of Physics, Beijing Normal University, Beijing 100875, China*

⁴*State Key Laboratory of Low-Dimensional Quantum Physics, Department of Physics, Tsinghua University, Beijing 100084, China*

⁵*Department of Physics, The Pennsylvania State University, University Park, Pennsylvania 16802, USA*

⁶*School of Physics and Wuhan National High Magnetic Field Center, Huazhong University of Science and Technology, Wuhan 430074, China*

⁷*CAS Center for Excellence in Topological Quantum Computation, University of Chinese Academy of Sciences, Beijing 100190, China*

⁸*Beijing Academy of Quantum Information Sciences, Beijing 100193, China*

⁹*Southern University of Science and Technology, Shenzhen 518055, China*

[#]These authors contribute equally

^{*}Correspondence to: jianwangphysics@pku.edu.cn (J.W.)

The nature of the anomalous metal, one of the quantum ground states of two-dimensional (2D) bosonic systems¹⁻⁵, remains a major puzzle even after several decades of study. The main characteristic of an anomalous metal is the saturation of the low-temperature resistance at a value far smaller than that predicted by the Drude formula^{1,2}. This calls into question whether the conventional understanding of metals is applicable to bosonic cases. Here, we report two types of bosonic metal states in ultrathin crystalline FeSe films grown on SrTiO₃, where the 2D high-temperature superconductivity is confined at the

interface. Our experiments are performed on pristine FeSe films and FeSe films with a triangular array of nano-holes. In pristine FeSe films, the bosonic anomalous metal state emerges at a high temperature (around 20 K), higher than all previous observations². In stark contrast, in nanopatterned FeSe films, the characteristic temperature of the anomalous metal state is considerably suppressed. In both types of FeSe films, we observe a linear-in-temperature (T -linear) resistance below onset temperature for superconductivity. Interestingly, the extremely large slope of this T -linear resistance, suppressed Hall coefficient and clear $h/2e$ quantum oscillations reveal the bosonic nature of the T -linear resistance, indicating a bosonic strange metal. Our discovery of the high-temperature anomalous metal state and the bosonic strange metal state in the 2D limit motivates further investigations aimed at unraveling the dissipation mechanism in bosonic metal states.

Conventional metals with low-lying fermionic excitations exhibit T^2 resistivities in the low temperature (T) regime as described by Fermi liquid theory⁶. Nevertheless, extensive studies of strongly correlated systems such as the cuprates⁷⁻⁹, pnictides^{10,11}, heavy fermion systems^{12,13}, and magic angle graphene¹⁴ have uncovered a new quantum state, the strange metal, which shows T -linear resistivity and anomalous thermodynamics. The strange metal is associated with the quantum criticality of unconventional superconductivity and magnetism, where pseudogap¹⁵, nematic order¹⁶, and ferromagnetic¹⁷ or antiferromagnetic¹⁸ order are suppressed. The properties of the strange metal are at odds with the expectations from Fermi liquid theory for weakly interacting quasiparticles and the origin has been a long-standing mystery¹⁹⁻²¹.

In superconductors, low-lying excitations are gapped out when electrons form Cooper pairs and condense into the quantum ground state. Governed by the Heisenberg uncertainty principle, there is phase and particle-number duality of Cooper pairs²². Thus, zero-resistance superconducting state with phase-coherent Cooper pairs and insulating state with localized Cooper pairs are believed to be the two ground states of two-dimensional (2D) superconductors²². However, when approaching zero temperature, a saturated finite resistance much smaller than the Drude value is detected, showing an anomalous metal state in 2D superconductor-

insulator/metal transitions, which challenges the prevailing consensus^{1,2}. The observation of linear current-voltage (*I*-*V*) curve further confirms the metallic characteristic²³⁻²⁷. The vanishing Hall coefficient^{23,28} and quantum oscillations with a period of one superconducting flux quantum $\frac{h}{2e}$ (*e* is the electron charge and *h* is the Planck's constant)²³ in the anomalous metal state suggest that bosonic low-lying excitations dominate the transport. The origin of the bosonic feature is still poorly understood^{1,2}, despite the ubiquitous observations of anomalous metal in a variety of 2D superconducting systems since 1989, including amorphous and granular films^{24,28-32}, crystalline films and nanodevices^{25-27,33-36}, superconducting arrays^{23,37-39}, and interfacial superconducting systems^{40,41}. Furthermore, other exotic metallic behavior of the bosonic low-lying excitation remains unexplored. Compared with the 2D superconducting systems mentioned above, the ultrathin FeSe crystalline films grown on SrTiO₃ (STO) substrate possess high-temperature interface superconductivity⁴²⁻⁴⁵, which emerges at the FeSe/STO interface and is localized in the first unit-cell FeSe on STO^{43,44}. The 2D nature of superconductivity has been justified by typical Berezinskii-Kosterlitz-Thouless (BKT) transition and the large anisotropy of the upper critical field⁴⁴. These features make the FeSe/STO a superior platform for the exploration of 2D bosonic metal states and the corresponding dissipation mechanisms.

Bosonic metal states in pristine FeSe/STO

In this paper, we report systematic transport measurements on ultrathin crystalline FeSe films down to one unit-cell thickness grown on STO substrates by molecular beam epitaxy. The scanning tunneling microscope (STM) images show tetragonal lattice structure of our FeSe film (Extended Data Fig. 1). For *ex-situ* transport measurements, we grew a series of macroscopic FeSe films (1-5 unit-cells thick) on pretreated insulating STO (001) substrates with protective FeTe capping layers (see Methods for details). The sheet resistance R_s versus temperature T curves of FeSe films reveal a superconductor to weakly localized metal transition with increasing normal state resistance (R_N) (Fig. 1a). The film with the smallest R_N (sample S1 in Fig. 1a) shows a superconducting state with zero-resistance within the measurement resolution at $T_c^{\text{zero}} = 17.4$ K and the onset superconducting critical temperature $T_c^{\text{onset}} = 46.6$ K (Extended Data Fig. 4b). Here, T_c^{onset} is defined as the temperature where the sheet resistance deviates from the linear extrapolation of the normal state,

and the normal state resistance is defined as $R_N = R_s(T_c^{\text{onset}})$. As R_N increases, the zero-resistance state fades away, accompanied by the appearance of small finite resistance (very close to zero for S2 in Fig. 1a), reminiscent of an anomalous metal state. When R_N further increases, the superconducting transition is broadened and terminates with a larger saturated resistance at lower temperatures (S3 and S4 in Fig. 1a). For FeSe films with R_N as high as $2 \text{ k}\Omega$ (S5 in Fig. 1a), the sheet resistance increases monotonically down to the lowest temperature, indicating an insulating-like behavior. We used the six-probe method to simultaneously measure the Hall (R_{yx}) and longitudinal resistance (R_s) for sample S3 (Fig. 1b). Above the superconducting transition, the small negative Hall coefficient indicates the heavy electron doping in the film, consistent with previous reports⁴⁶. Below T_c^{onset} , the Hall coefficient (R_{yx}/B , B is the magnetic field) drops with decreasing temperature and reaches zero within the measurement resolution below 20 K while R_s remains finite, indicating that Cooper pairs (bosons) dominate the transport behavior of the metallic states at low temperatures^{23,28}.

Figures 1c and 1d present the Arrhenius plots of the anomalous metal state under different perpendicular and parallel magnetic fields, respectively. Surprisingly, the anomalous metal state persists up to $T^{\text{AM}} = 19.7 \text{ K}$ (56.1% of T_c^{onset}) at zero magnetic field, which is much higher than previous reports². An external magnetic field up to 15 T in the perpendicular direction (B_{\perp}) broadens the superconducting transition and reduces T^{AM} from 19.7 K to 7.0 K (Fig. 1c). In contrast, a parallel field (B_{\parallel} , along the in-plane direction of the film) hardly affects the resistance drop and only changes T^{AM} from 19.7 K at 0 T to 15.0 K at 15 T (Fig. 1d). The high-temperature anomalous metal state is confirmed in another representative FeSe film on STO (Extended Data Fig. 3). In previous studies of conventional superconductors, the anomalous metal state only exists over a temperature scale of hundreds of millikelvin^{25,28,31,35-40} (see Fig. 1e). In high-temperature cuprate superconductors (e.g. $\text{La}_2\text{CuO}_{4+\delta}$ and nanopatterned $\text{YBa}_2\text{Cu}_3\text{O}_{7-x}$ films, the open orange circles in Fig. 1e), the anomalous metal state is reported up to $\sim 10 \text{ K}$, corresponding to a relatively small ratio of $T^{\text{AM}}/T_c^{\text{onset}}$. A large $T^{\text{AM}}/T_c^{\text{onset}}$ ratio is commonly seen in interface superconductors, however, these systems usually show a low T^{AM} (e.g. LAO/KTO and LAO/STO, the blue diamond dots in Fig. 1e). Therefore, the extremely high T^{AM} accompanied by the large ratio of

$T_{\text{AM}}/T_c^{\text{onset}}$ in ultrathin FeSe films (the open orange diamond in Fig. 1e) are striking in this context and suggestive of a large energy scale associated with the anomalous metal state in FeSe/STO systems.

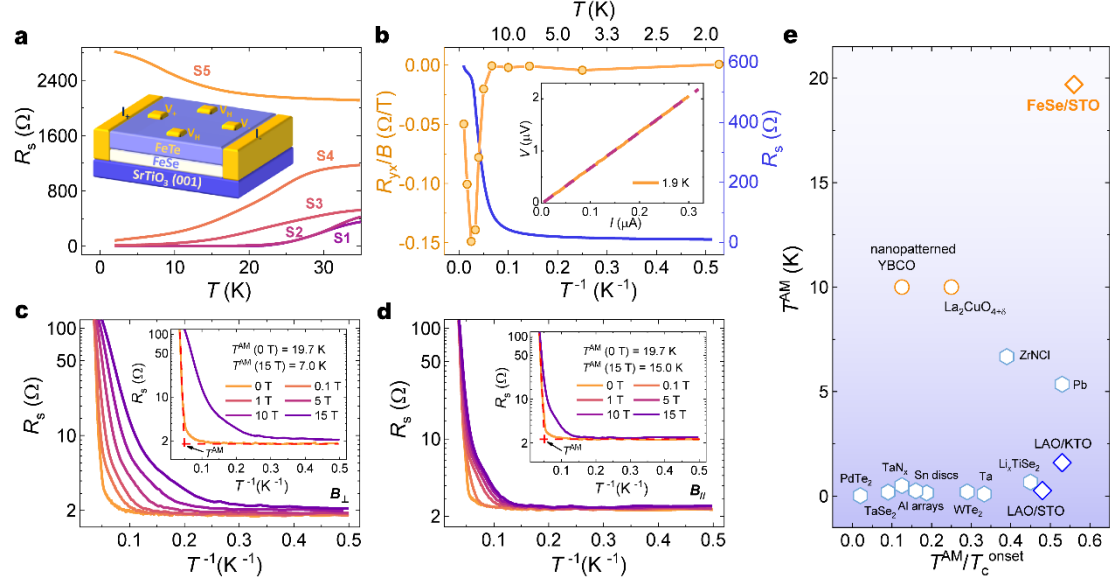


Fig. 1 | High-temperature anomalous metal state in FeSe/STO. **a**, Temperature dependent sheet resistance $R_s(T)$ of FeSe/STO sample S1 to S5 with different normal state resistances, showing superconductor-anomalous metal-weakly localized metal transitions. Inset is a schematic for six-probe transport measurements on FeSe/STO. **b**, The $R_s(T)$ curve (the blue curve) and the Hall coefficient R_{yx}/B (the yellow dots) of sample S3. Inset is an I - V curve at 1.9 K showing a linear behavior below 300 nA. The excitation current for $R_s(T)$ measurements is 100 nA, which is within the ohmic region. **c, d**, Arrhenius plots of $R_s(T)$ curves under perpendicular magnetic fields and parallel fields, showing an anomalous metal state with onset temperature (T_{AM}) up to 19.7 K. T_{AM} is the temperature where anomalous metal state appears, defined as the crossing point of the extrapolation of resistance drop and saturation as shown in the insets of Fig. 1c, d. **e**, Overview of T_{AM} and the ratio $T_{\text{AM}}/T_c^{\text{onset}}$ of various 2D superconducting systems, including amorphous and granular films^{28,29,31}, crystalline films and nanodevices^{25,33-36}, superconducting arrays^{23,38,39}, and interfacial superconducting systems^{40,41}. The FeSe/STO in this paper is indicated by a yellow diamond dot. The highest values of T_{AM} and $T_{\text{AM}}/T_c^{\text{onset}}$ from each 2D superconducting system are shown in this panel.

In the wide superconducting transition region of FeSe films with a larger normal state resistance, we observe an extraordinary linear-in-temperature resistance below T_c^{onset} , representing a key signature of the strange metal. Figure 2 summarizes the T -linear resistance under both perpendicular and parallel magnetic fields. The T -linear resistance extends to lower temperatures (Fig. 2a, d, g), and the temperature regime of T -linear resistance ($\Delta T/T_c^{\text{onset}}$) grows (Fig. 2b, e, h) when the external field is relatively small. We fit the $R_s(T)$ curves at various magnetic fields for different films using the power law equation $R_s(T) = a + bT^n$, where a , b and n are fitting coefficients. As shown in Extended Data Table 1, n is around 1 for most $R_s(T)$ curves, verifying the T -linear resistance. Under a higher magnetic field, T_c^{onset} decreases and the temperature regime of strange metal state shrinks with n deviating from 1.

The slopes of T -linear resistance below T_c^{onset} are summarized in Fig. 2c, f, i. At zero field, the slope of the FeSe film is around 34-120 Ω/K , an extremely large value compared with previous observations of fermionic strange metals. To be specific, the slope α_F for high-temperature cuprate superconductors (e.g. $\text{La}_{2-x}\text{Sr}_x\text{CuO}_4$, $\text{Pr}_{2-x}\text{Ce}_x\text{CuO}_{4\pm\delta}$, and $\text{La}_{2-x}\text{Ce}_x\text{CuO}_4$) lies in the range 1.7-8.2 Ω/K ⁸. Furthermore, recent studies report that α_F is even smaller ($\sim 0.13 \Omega/\text{K}$) in pulsed-laser deposition grown thick FeSe films⁴⁷. In our measurements, above T_c^{onset} one typical 1-UC FeSe/STO shows T -linear resistance with the slope of 1.23 Ω/K (Extended Data. Fig. 4b). Therefore, a fermionic strange metal state cannot explain the large slope observed in our FeSe films below T_c^{onset} . Additionally, the Hall coefficient is significantly suppressed with decreasing temperature in the temperature regime of T -linear resistance (Extended Data Fig. 2). Thus, the strange metal state below T_c^{onset} very likely originates from the transport of Cooper pairs (bosons) rather than quasiparticles (fermions). In the fermionic strange metal, a dimensionless coefficient $\eta_F = \frac{2e^2}{h} \cdot \alpha_F \cdot T_F$ can be defined for the slope α_F of T -linear resistance where T_F is the Fermi temperature and η_F is around 0.2-1.6, as revealed by previous experimental studies^{8,14}. Here, in our system, the T -linear resistance manifests below T_c^{onset} , allowing us to define an effective coefficient by analogy. We represent the characteristic energy scale for Cooper pairs by T_c^{onset} , leading to $\eta_B = \frac{2e^2}{h} \cdot \alpha_B \cdot T_c^{\text{onset}}$. The typical value

of η_B is around 0.2 in our films with T -linear resistance, giving rise to a large value of α_B . As shown in Fig. 2c, f, i, α_B firstly increases and then decreases, showing opposite behavior to $\Delta T/T_c^{\text{onset}}$ with increasing magnetic field.

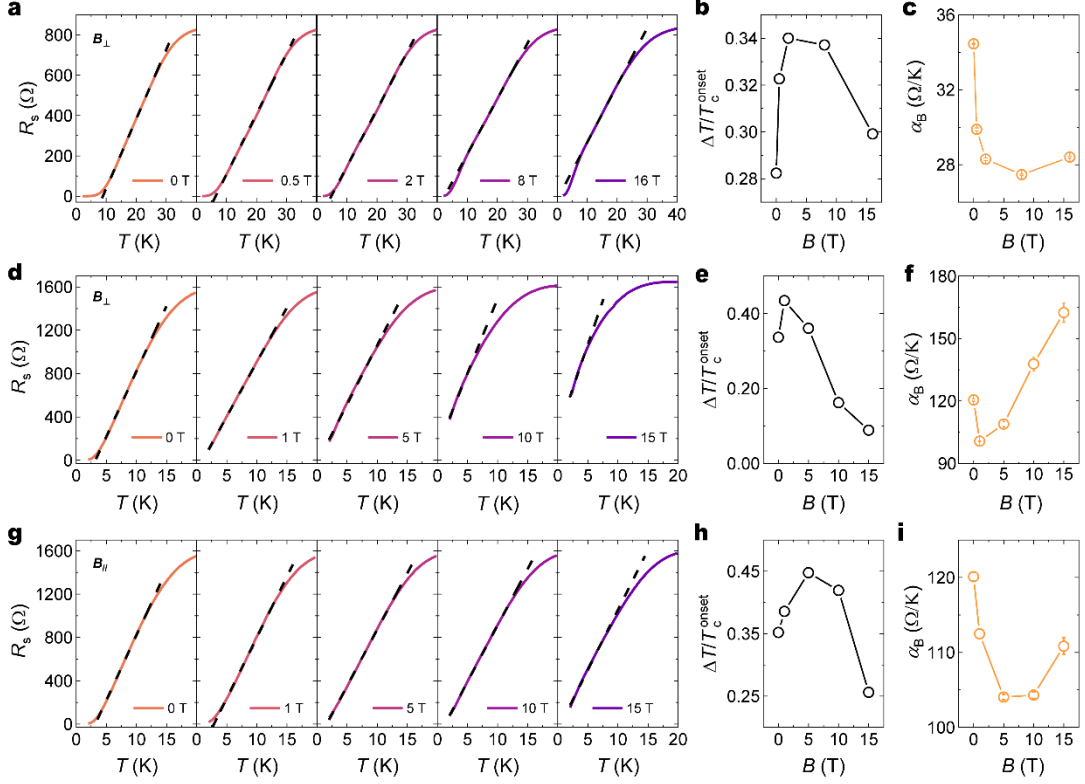


Fig. 2 | T -linear resistance of FeSe/STO below T_c^{onset} . **a, d, g**, The $R_s(T)$ curves under perpendicular (**a** (S7), **d** (S8)) and parallel (**g** (S8)) magnetic fields. The black dashed lines are fits to the linear part of $R_s(T)$ curves, indicating a strange metal state. The linearity of $R_s(T)$ curves is further examined with power fitting, $R_s(T) = a + bT^n$ (Extended Data Table 1). **b, e, h**, Field dependence of the temperature ratio ($\Delta T/T_c^{\text{onset}}$), ΔT is the temperature range of the linear $R_s(T)$ curves. **c, f, i**, The slopes α_B of linear $R_s(T)$ under different fields in **a, d** and **g**.

To further explore the nature of the bosonic metal states in FeSe/STO systems below T_c^{onset} , we tune the disorder strength of FeSe/STO by fabricating a triangular array of nano-holes. Specifically, the superconducting FeSe/STO samples (~ 2 unit-cells of FeSe with FeTe protection layers) are etched through a contact mask via reactive ion etching (RIE) (see Methods for details). The patterns, which have ~ 70 nm

diameter holes arranged in a triangular array with center-to-center spacing of ~ 102 nm, are transferred onto the FeSe films (see Extended Data Fig. 5 for a scanning electronic microscope image of the patterns). The intermediate triangular superconducting areas (marked as island in Fig. 3b) between the nano-holes connect to each other through the insulating links, forming a Josephson junction array (JJA) of FeSe/STO (Fig. 3b). A longer etching time induces more damage through the sidewall of the nano-holes and makes the links between superconducting areas more resistive, which increases R_N and the disorder strength (Fig. 3a).

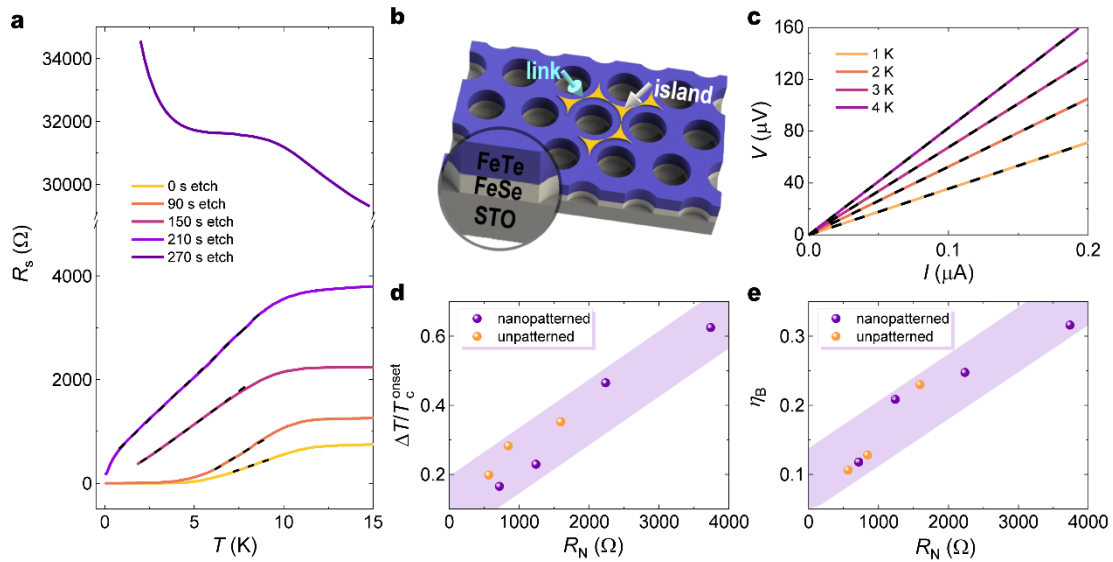


Fig. 3 | T -linear resistance of nanopatterned FeSe/STO with triangular arrays of nano-holes. **a**, The $R_s(T)$ curves of FeSe films with different etching times measured with 100 nA. A shorter etching time corresponds to a smaller normal state resistance (R_N) and narrower range of linear $R_s(T)$. The linear $R_s(T)$ trend persists down to 1 K for 210 s etched film. The black dashed lines are linear fits to $R_s(T)$. **b**, Schematic for nanopatterned FeSe film on STO substrate. Superconducting areas (marked as island) are connected by insulating links. **c**, The I - V curves showing ohmic behavior within 200 nA down to 1 K for 210 s etched film. **d, e**, $\Delta T/T_c^{\text{onset}}$ (ΔT is temperature range of the linear part of $R_s(T)$ curves) and η_B as a function of normal state resistance (R_N) at zero field for both unpatterned (S3 in Fig. 1a, S7 and S8 in Fig. 2) and nanopatterned films. $\Delta T/T_c^{\text{onset}}$ and η_B both exhibit positive correlation with R_N . The shadow areas are guides for the eye.

Bosonic metal states in nanopatterned FeSe/STO

The superconducting transition region gets wider as R_N increases. Meanwhile, below T_c^{onset} a remarkably T -linear resistance temperature range (Fig. 3a) appears and extends with the increasing etching time from 90 s ($R_N = 1.2 \text{ k}\Omega$) to 210 s ($R_N = 3.7 \text{ k}\Omega$). The film with the etching time of 270 s shows insulating behavior at low temperatures (R_N is as high as $31.5 \text{ k}\Omega$). Note that we use a small excitation current (100 nA) within the linear (*i.e.*, ohmic) regime of the I - V curve of FeSe/STO (Fig. 3c); this allows access to the intrinsic metallic transport properties of the FeSe films below T_c^{onset} . In Fig. 3d, e, we plot $\Delta T/T_c^{\text{onset}}$ and η_B of the T -linear resistance against R_N in both unpatterned and nanopatterned films. Both $\Delta T/T_c^{\text{onset}}$ and η_B increase with increasing R_N , revealing that the large disorder strength generically expands the temperature regime of T -linear resistance, the main signature of the bosonic strange metal state. This behavior appears to be insensitive to the microscopic details of the disorder.

We also performed ultralow temperature transport measurements down to 50 mK. The 0 s and 90 s etched film exhibit a zero-resistance state at low temperatures, while 210 s etched film shows a finite resistance down to 50 mK. For the 210 s etched film, the I - V measurements show ohmic behavior within 40 nA in the ultralow temperature regime down to 50 mK (Fig. 4a). The saturation of the resistance below 100 mK signals an anomalous metal state (Fig. 4b). Previous studies suggest that external high frequency noise may disrupt the coherence of superconductivity at ultralow temperatures and cause artificial resistance saturation^{26,48,49}. To exclude these effects, the measurements were carried out in a dilution refrigerator cryostat with radio frequency filters. $R_s(T)$ curves show that the resistance saturation at low temperatures remains the same when the excitation current is within the linear regime (below 40 nA) of the I - V curves Fig. 4a. When applying a perpendicular magnetic field, the saturated resistance increases with increasing field (Fig. 4c), quite similar to the behavior of the high-temperature anomalous metal state in unpatterned FeSe films (Fig. 1c). The anomalous metal state also displays a giant positive longitudinal magnetoresistance (Fig. 4d), which is gradually smeared out at higher temperatures. Furthermore, within $\pm 0.8 \text{ T}$ the magnetoresistance oscillates with a monotonically rising background, as

shown in Fig. 4e. The oscillation field period, ~ 0.221 T, is consistent with one superconducting flux quantum $\phi_0 = \frac{h}{2e}$ threading an area of one unit cell of the nanopattern (around 9010 nm^2) in the JJA (e is the electron charge), indicating that Cooper pairs dominate the anomalous metal state. The $h/2e$ quantum oscillations persist up to 4 K (Fig. 4e, f), which is within the temperature regime of T -linear resistance, further demonstrating the bosonic nature of the observed strange metal state.

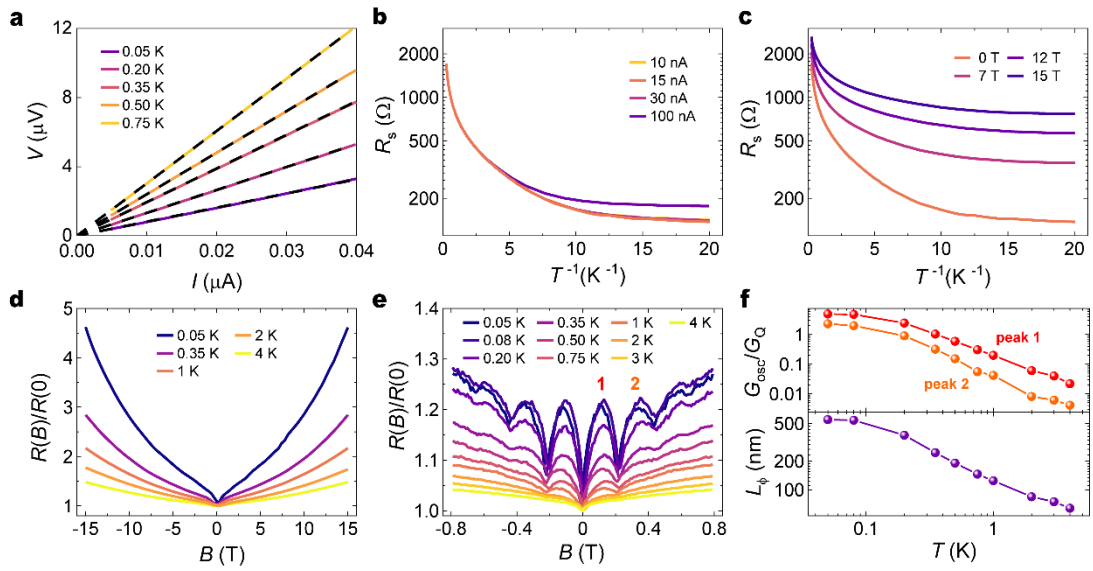


Fig. 4 | Anomalous metal state in nanopatterned FeSe/STO (210 s etched film). **a**, I - V curves at temperatures from 0.05 K to 0.75 K. The linear behavior maintains up to 40 nA. **b**, Arrhenius plots of $R_s(T)$ curves under different currents. **c**, Arrhenius plots of $R_s(T)$ curves under different magnetic fields, measured at 15 nA. **d**, Giant positive magnetoresistance at various temperatures from -15 T to 15 T. **e**, Magnetoresistance from -0.8 T to 0.8 T, showing quantum oscillations. The oscillation period is around ~ 0.221 T, corresponding to one superconducting flux quantum for a unit cell pattern of 9010 nm^2 . **f**, The amplitude of magnetoconductance oscillations G_{osc} (upper panel, the corresponding peak levels are indicated in **e**) and the phase coherence length L_ϕ (lower panel, derived from magnetoconductance oscillations of peak 2) as a function of temperature (see Methods for details).

Discussion

Figure 5 presents the schematic phase diagrams of unpatterned and nanopatterned FeSe films. Below T_c^{onset} , we identify the superconducting state (zero resistance within the measurement resolution), the anomalous metal state (resistance saturation at low temperatures), and the bosonic strange metal state (T -linear resistance). When approaching zero temperature, the weakly localized metal and insulator phases show increasing resistance below and above the quantum resistance for Cooper pairs ($h/4e^2=6.45$ k Ω), respectively. In Fig. 5a, the unpatterned FeSe film undergoes a superconductor-anomalous metal transition with increasing R_N . The temperature regime of the anomalous metal state can be very large, comparable to the superconducting state region. In contrast, the bosonic strange metal state exists only in a stripe area of the schematic phase diagram. With increasing R_N , the temperature regime of the bosonic strange metal first grows and then shrinks. Finally, the unpatterned FeSe film becomes a weakly localized metal. The bosonic nature of the anomalous metal state is demonstrated by the zero Hall coefficient (Fig. 1b) and a giant magnetoresistance (Extended Data Fig. 8). The bosonic strange metal state is characterized by the extremely large slope of $R_s(T)$ curves and suppressed Hall coefficients, compared with that of the fermionic strange metal (Fig. 2c, f, i). In Fig. 5b, the nanopatterned FeSe film shows a superconductor to anomalous metal transition, followed by an anomalous metal to insulator transition. The temperature regime of anomalous metal state is relatively small, while the bosonic strange metal state occupies a large area in the phase diagram. The $\frac{h}{2e}$ quantum oscillations exist in the anomalous metal (Fig. 4e), bosonic strange metal (Fig. 4e), and insulator (Extended Data Fig. 6) phases, indicating that Cooper pairs dominate the transport of these states.

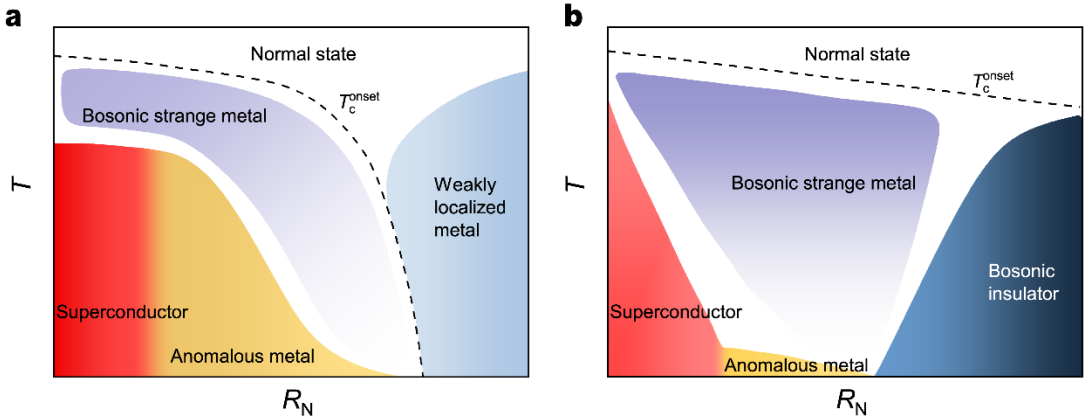


Fig. 5 | The schematic phase diagrams of unpatterned FeSe/STO (a) and FeSe/STO JJA samples (b). Below T_c^{onset} , superconductor, anomalous metal, and bosonic strange metal are characterized by zero resistance within the instrument resolution, residual resistance plateau, and T -linear resistance, respectively. Weakly localized metal and insulator show increasing resistance as $T \rightarrow 0$. With increasing R_N (representing the disorder), the unpatterned FeSe/STO shows superconductor-anomalous metal transition (a). With further increasing R_N , the unpatterned FeSe/STO becomes a weakly localized metal. The anomalous metal can persist up to a high-temperature, comparable to the zero-resistance superconducting transition temperature showing large $T^{\text{AM}}/T_c^{\text{onset}}$ values (see Fig. 1a). With increasing R_N (representing the disorder), the FeSe/STO JJA sample shows superconductor-anomalous metal-insulator transitions in b. The $T^{\text{AM}}/T_c^{\text{onset}}$ value of anomalous metal state in FeSe/STO JJA sample is small ($\sim 3.2\%$). The resistance of the weakly localized metal phase is much smaller than that of the bosonic insulator phase.

Finally, we discuss our theoretical understanding of the bosonic strange metal state in nanopatterned FeSe films. The T -linear resistance in the strange metal has been proposed previously⁵⁰ and later grounded by microscopic theoretical analysis of the dissipative quantum XY model^{19,51,52}. In this picture, phase factor damping is the key to understanding the bosonic strange metal state. A heuristic argument relates the T -linear resistance to the incoherent precession of the local phase of the Cooper pairs.

This leads to an electric field originating in the temporal gradient $\vec{E} = -\frac{\partial \vec{A}}{\partial t}$. Using London's equation $j_s = -\frac{n_s(t)(2e)^2 \vec{A}}{m^*}$ with $n_s(t) = n_{\text{cp}} e^{-t/\tau}$ denoting the incoherent

boson density, one can obtain the resistivity with a Drude form: $R_{\text{cp}} \simeq \frac{m^*}{n_{\text{cp}}(2e)^2} \frac{1}{\tau}$. Here τ is the characteristic damping time and has been obtained previously. For the JJA model, $\frac{1}{\tau}$ is proportional to the temperature T around the critical link resistance^{53,54}. The observations of T -linear resistance in nanopatterned FeSe/STO samples are consistent with this heuristic analysis.

Our observation of the bosonic strange metal state in high-temperature unpatterned crystalline superconducting films (FeSe/STO) presents a greater theoretical challenge since it requires going beyond the understanding based on the JJA model. In our experiments, in both pristine and patterned FeSe samples, $\Delta T/T_c^{\text{onset}}$ and η_B of the bosonic strange metal state increase with increasing normal state resistance, showing nearly the same dependence on disorder strength as shown in Fig. 3d, e. These experimental results indicate that the bosonic strange metal states in high-temperature unpatterned crystalline superconducting films and JJA only depend on the total disorder strength and not the microscopic details of disorder. Further theoretical investigations are needed to clarify the origin of T -linear resistance in crystalline samples, especially the relation to the dynamics of phase factor for general bosonic systems^{19,51,52,55}.

The anomalous metal state in unpatterned crystalline FeSe/STO has distinct properties when compared with previous studies of anomalous metal behavior in various 2D superconductors and high-temperature superconductors. Figure 1e indicates that high-temperature superconductors normally have a high T^{AM} and the interface superconductors exhibit a large $T^{\text{AM}}/T_c^{\text{onset}}$. FeSe/STO, a high-temperature interface superconductor in the 2D limit, has both the highest T^{AM} and the largest $T^{\text{AM}}/T_c^{\text{onset}}$ so far, presenting a qualitatively new platform to explore the underlying mechanism of the anomalous metal state. The enhancement of $T^{\text{AM}}/T_c^{\text{onset}}$ for interface superconductors may relate to a novel dissipation mechanism, disorder, or doping effect at the interface.

In comparison, for nanopatterned FeSe/STO, the $T^{\text{AM}}/T_c^{\text{onset}}$ of the anomalous metal state turns out to be very small (around 3.2%), revealing that the anomalous metal state is sensitive to the microscopic details of disorder. The bosonic anomalous metal phases are qualitatively consistent with theoretical predictions of a quasi-

ordered phase with ultraslow dynamics for the phase factor in the dissipative quantum XY model^{19,52}. One typical example with the ultraslow dynamics is the glassy systems with replica symmetry breaking⁵⁶. The anomalous metal states in both unpatterned and nanopatterned FeSe/STO samples call for theoretical endeavors to investigate whether or not replica symmetry breaking plays a dominant role in the ultraslow dynamics of the phase factor.

Reference

1. Phillips, P. & Dalidovich, D. The elusive Bose metal. *Science* **302**, 243-247 (2003).
2. Kapitulnik, A., Kivelson, S. A. & Spivak, B. Colloquium: Anomalous metals: Failed superconductors. *Rev. Mod. Phys.* **91**, 011002 (2019).
3. Saito, Y., Nojima, T. & Iwasa, Y. Highly crystalline 2D superconductors. *Nat. Rev. Mater.* **2**, 16094 (2016).
4. Sacépé, B., Feigel'man, M. & Klapwijk, T. M. Quantum breakdown of superconductivity in low-dimensional materials. *Nat. Phys.* **16**, 734-746 (2020).
5. Das, D. & Doniach, S. Existence of a Bose metal at $T=0$. *Phys. Rev. B* **60**, 1261-1275 (1999).
6. Landau, L. D. The theory of a Fermi liquid. *Sov. Phys. JETP* **3**, 920–925 (1957).
7. Martin, S., Fiory, A. T., Fleming, R. M., Schneemeyer, L. F. & Waszczak, J. V. Normal-state transport properties of $\text{Bi}_{2+x}\text{Sr}_{2-y}\text{CuO}_{6\pm\delta}$ crystals. *Phys. Rev. B* **41**, 846-849 (1990).
8. Legros, A. et al. Universal T-linear resistivity and Planckian dissipation in overdoped cuprates. *Nat. Phys.* **15**, 142-147 (2019).
9. Michon, B. et al. Thermodynamic signatures of quantum criticality in cuprate superconductors. *Nature* **567**, 218-222 (2019).
10. Doiron-Leyraud, N. et al. Correlation between linear resistivity and T_c in the Bechgaard salts and the pnictide superconductor $\text{Ba}(\text{Fe}_{1-x}\text{Co}_x)_2\text{As}_2$. *Phys. Rev. B* **80**, 214531 (2009).
11. Analytis, J. G. et al. Transport near a quantum critical point in $\text{BaFe}_2(\text{As}_{1-x}\text{P}_x)_2$. *Nat. Phys.* **10**, 194-197 (2014).
12. Custers, J. et al. The break-up of heavy electrons at a quantum critical point. *Nature* **424**, 524-527 (2003).
13. Bruin, J. A. N., Sakai, H., Perry, R. S. & Mackenzie, A. P. Similarity of scattering rates in metals showing T-Linear resistivity. *Science* **339**, 804-807 (2013).
14. Cao, Y. et al. Strange metal in magic-angle graphene with near Planckian dissipation. *Phys. Rev. Lett.* **124**, 076801 (2020).
15. Daou, R. et al. Linear temperature dependence of resistivity and change in the Fermi surface at the pseudogap critical point of a high- T_c superconductor. *Nat. Phys.* **5**, 31-34 (2009).
16. Licciardello, S. et al. Electrical resistivity across a nematic quantum critical point. *Nature* **567**, 213-217 (2019).
17. Shen, B. et al. Strange-metal behaviour in a pure ferromagnetic Kondo lattice. *Nature* **579**, 51-55 (2020).
18. Gegenwart, P., Si, Q. & Steglich, F. Quantum criticality in heavy-fermion metals. *Nat. Phys.* **4**, 186-197 (2008).
19. Varma, C. M. Colloquium: Linear in temperature resistivity and associated mysteries including high temperature superconductivity. *Rev. Mod. Phys.* **92**, 031001 (2020).
20. Sachdev, S. *Quantum phase transitions* (Cambridge university press, 2011).
21. Hartnoll, S. A., Andrew Lucas, and Subir Sachdev. *Holographic quantum matter* (MIT press, 2018).
22. Phillips, P. *Advanced Solid State Physics* (Cambridge University Press, 2012).

23. Yang, C. et al. Intermediate bosonic metallic state in the superconductor-insulator transition. *Science* **366**, 1505 (2019).
24. Ienaga, K., Hayashi, T., Tamoto, Y., Kaneko, S. & Okuma, S. Quantum criticality inside the anomalous metallic state of a disordered superconducting thin film. *Phys. Rev. Lett.* **125**, 257001 (2020).
25. Liu, Y. et al. Type-II Ising superconductivity and anomalous metallic state in macro-size ambient-stable ultrathin crystalline films. *Nano Lett.* **20**, 5728-5734 (2020).
26. Xing, Y. et al. Extrinsic and intrinsic anomalous metallic states in transition metal dichalcogenide Ising superconductors. *Nano Lett.* **21**, 7486-7494 (2021).
27. Li, L. et al. Anomalous quantum metal in a 2D crystalline superconductor with electronic phase nonuniformity. *Nano Lett.* **19**, 4126-4133 (2019).
28. Breznay, N. P. & Kapitulnik, A. Particle-hole symmetry reveals failed superconductivity in the metallic phase of two-dimensional superconducting films. *Sci. Adv.* **3**, e1700612 (2017).
29. Jaeger, H. M., Haviland, D. B., Orr, B. G. & Goldman, A. M. Onset of superconductivity in ultrathin granular metal films. *Phys. Rev. B* **40**, 182-196 (1989).
30. Yazdani, A. & Kapitulnik, A. Superconducting-insulating transition in two-dimensional α -MoGe thin films. *Phys. Rev. Lett.* **74**, 3037-3040 (1995).
31. Qin, Y., Vicente, C. L. & Yoon, J. Magnetically induced metallic phase in superconducting tantalum films. *Phys. Rev. B* **73**, 100505 (2006).
32. Wang, Y., Tamir, I., Shahar, D. & Armitage, N. P. Absence of cyclotron resonance in the anomalous metallic phase in InO_x . *Phys. Rev. Lett.* **120**, 167002 (2018).
33. Garcia-Barriocanal, J. et al. Electronically driven superconductor-insulator transition in electrostatically doped $\text{La}_2\text{CuO}_{4+\delta}$ thin films. *Phys. Rev. B* **87**, 024509 (2013).
34. Saito, Y., Kasahara, Y., Ye, J., Iwasa, Y. & Nojima, T. Metallic ground state in an ion-gated two-dimensional superconductor. *Science* **350**, 409 (2015).
35. Liao, M. et al. Coexistence of resistance oscillations and the anomalous metal phase in a lithium intercalated TiSe_2 superconductor. *Nat. Commun.* **12**, 5342 (2021).
36. Sajadi, E. et al. Gate-induced superconductivity in a monolayer topological insulator. *Science* **362**, 922-925 (2018).
37. Eley, S., Gopalakrishnan, S., Goldbart, P. M. & Mason, N. Approaching zero-temperature metallic states in mesoscopic superconductor–normal–superconductor arrays. *Nat. Phys.* **8**, 59-62 (2012).
38. Han, Z. et al. Collapse of superconductivity in a hybrid tin–graphene Josephson junction array. *Nat. Phys.* **10**, 380-386 (2014).
39. Bøtcher, C. G. L. et al. Superconducting, insulating and anomalous metallic regimes in a gated two-dimensional semiconductor–superconductor array. *Nat. Phys.* **14**, 1138-1144 (2018).
40. Chen, Z. et al. Carrier density and disorder tuned superconductor-metal transition in a two-dimensional electron system. *Nat. Commun.* **9**, 4008 (2018).
41. Chen, Z. et al. Electric field control of superconductivity at the $\text{LaAlO}_3/\text{KTaO}_3(111)$ interface. *Science* **372**, 721 (2021).
42. Huang, D. & Hoffman, J. E. Monolayer FeSe on SrTiO_3 . *Annu. Rev. Condens. Matter Phys.* **8**, 311-336 (2017).
43. Wang, Q.-Y. et al. Interface-induced high-temperature superconductivity in

single unit-cell FeSe films on SrTiO_3 . *Chin. Phys. Lett.* **29**, 037402 (2012).

44. Zhang, W.-H. et al. Direct observation of high-temperature superconductivity in one-unit-cell FeSe films. *Chin. Phys. Lett.* **31**, 017401 (2014).

45. Wang, Z., Liu, C., Liu, Y. & Wang, J. High-temperature superconductivity in one-unit-cell FeSe films. *J. Condens. Matter Phys.* **29**, 153001 (2017).

46. Wang, Q. et al. Thickness dependence of superconductivity and superconductor-insulator transition in ultrathin FeSe films on SrTiO_3 (001) substrate. *2D Mater.* **2**, 044012 (2015).

47. Jiang, X. et al. Enhancement of superconductivity linked with linear-in-temperature/field resistivity in ion-gated FeSe films. Preprint at <https://arxiv.org/abs/2103.06512> (2021).

48. Tamir, I. et al. Sensitivity of the superconducting state in thin films. *Sci. Adv.* **5**, eaau3826 (2019).

49. Shin, J., Park, S. & Kim, E. Effect of external electromagnetic radiation on the anomalous metallic behavior in superconducting Ta thin films. *Phys. Rev. B* **102**, 184501 (2020).

50. Varma, C. M., Littlewood, P. B., Schmitt-Rink, S., Abrahams, E. & Ruckenstein, A. E. Phenomenology of the normal state of Cu-O high-temperature superconductors. *Phys. Rev. Lett.* **63**, 1996-1999 (1989).

51. Aji, V. & Varma, C. M. Theory of the quantum critical fluctuations in cuprate superconductors. *Phys. Rev. Lett.* **99**, 067003 (2007).

52. Zhu, L., Hou, C. & Varma, C. M. Quantum criticality in the two-dimensional dissipative quantum XY model. *Phys. Rev. B* **94**, 235156 (2016).

53. Chakravarty, S. & Leggett, A. J. Dynamics of the two-state system with ohmic dissipation. *Phys. Rev. Lett.* **52**, 5-8 (1984).

54. Leggett, A. J. et al. Dynamics of the dissipative two-state system. *Rev. Mod. Phys.* **59**, 1-85 (1987).

55. Lindner, N. H. & Auerbach, A. Conductivity of hard core bosons: A paradigm of a bad metal. *Phys. Rev. B* **81**, 054512 (2010).

56. Mézard, M., Giorgio Parisi, and Miguel Angel Virasoro. in *Spin glass theory and beyond: An Introduction to the Replica Method and Its Applications* Vol. 9 (World Scientific Publishing Company, 1987).

Methods

Film growth

Thin FeSe films (1-5 unit-cells) were epitaxially grown in an ultra-high vacuum molecular beam epitaxy (MBE) chamber. Pretreated single crystal STO (001) substrates were used for the growth⁴⁴. We etched the substrates with deionized water (90 °C, 45 min) and 10% HCl solution (room temperature, 45 min). Then, we annealed the substrates in a tube furnace under oxygen flow at 980 °C for 3 h. Before growth, the substrates were degassed at 600 °C for 0.5 h in MBE chamber. Through the above treatments, the STO (001) surface became atomically flat with step terrace structure and TiO₂ termination. FeSe films were then grown by co-evaporating Fe (99.995%) and Se (99.9999%) from Knudsen cells with a flux ratio of ~1:10 as the substrates were heated to 400 °C. After growth, FeSe films were gradually annealed up to 450 °C. To protect the thin FeSe films from oxidization, FeTe protection layers were grown by co-evaporating Fe (99.995%) and Te (99.9999%) with a flux ratio of ~1:4 at 270 °C. During the growth, scanning tunneling microscope was used to examine the morphology and crystal quality of the films. Our films are rectangular strips around 6 mm long and 2 mm wide, grown on substrates in 2 mm × 10 mm.

The fabrication of nano-holes array

To fabricate Josephson junction array on FeSe/STO, we etched the FeSe films by reactive ion etching (RIE) technique through anodic aluminum oxide (AAO) membrane masks. The AAO mask, with a triangular array of holes (70 nm in diameter and 100 nm in period), was transferred onto the FeSe film in acetone²³. The etching was performed with Ar flow (20 sccm) and 200 W radio frequency power. The chamber pressure was kept around 6.0 Pa during etching. With increasing etching time, the normal state resistance increases and the film changes from superconducting state to anomalous metal and then insulating state.

Transport measurements

The six-probe configuration was used for the transport measurements, as shown in the inset of Fig. 1a. Two indium strips (I_+ and I_-) were pressed along the width of the film so that the current could homogeneously pass through the sample. The other four indium electrodes acted as the voltage probes. Two of them (V_+ and V_-) were used to

measure the longitudinal voltage and another two electrodes (V_H) were Hall electrodes. In our measurements under parallel magnetic fields, the fields were orthogonal to the current excitations. The temperature-dependent resistance and magnetoresistance were measured in a Physical Property Measurement System (*Quantum Design*). Ultra-low temperature measurements down to 50 mK were carried out in a dilution refrigerator option with radio frequency filters (*Quantum Design*).

Exclusion of classical percolation model for anomalous metal state

The anomalous metal state in FeSe/STO interface superconductor exhibits various interesting phenomena, including resistance saturation at low temperatures, zero Hall resistance, large magnetoresistance and linear I - V curves. These features cannot be explained by the classical percolation model², where the local superconducting regions are embedded in the normal state. In such case, although the combination of the zero-resistance superconducting and normal state regions may satisfy the requirement of linear I - V curve, large magnetoresistance is not expected (the magnetoresistance is very small for the normal state as presented in Extended Data Fig. 8) and vice versa, which thus are inconsistent with our observations. In addition, the classical percolation model, in which the finite resistance is contributed by the normal state, is contradict to the observation of zero Hall resistance²⁸. Therefore, the above discussion demonstrates that the classical percolation model can be excluded.

Quantum oscillations in nanopatterned FeSe/STO

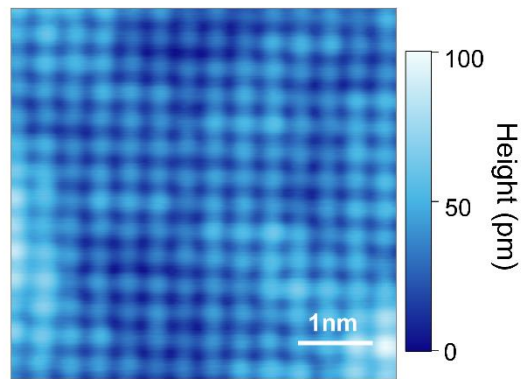
The $h/2e$ oscillations are observed in both the anomalous metal state and the insulating state (Extended Data Fig. 6 and Extended Data Fig. 7), which demonstrates that Cooper pairs dominate the transport in these states. The temperature dependence of the oscillation amplitude is extracted as $G_{\text{osc}} = \left| G\left(\frac{B_0}{2}\right) - G_0 \right|$ after subtracting the background, where G_0 and $G\left(\frac{B_0}{2}\right)$ are the conductance of peak and dip of each oscillation, as shown in Fig. 4f. The phase coherence length (L_ϕ) of Cooper pairs is estimated by $G_{\text{osc}} = \frac{4e^2}{h} \left(\frac{L_\phi}{\pi r}\right)^{1.5} \exp\left(-\frac{\pi r L_\phi}{L_\phi}\right)$ ²³. G_Q is the quantum conductance for Cooper pairs, $\frac{4e^2}{h}$. G_{osc} and L_ϕ saturate at low temperatures (Fig. 4f), reminiscent of the anomalous metal state in nanopatterned $\text{YBa}_2\text{Cu}_3\text{O}_{7-x}$ films²³.

Acknowledgements We thank Yanzhao Liu and Ying Xing for helpful discussions. We thank Xucun Ma, Guanyang He and Yue Tang for the help in sample fabrication and characterization. This work was financially supported by the National Natural Science Foundation of China (Grant No. 11888101), the National Key Research and Development Program of China (Grant No. 2018YFA0305604, No. 2017YFA0303300), the National Natural Science Foundation of China (No. 11774008, No. 51788104, No. 12074210, No. 12174442), Beijing Natural Science Foundation (Z180010), the Strategic Priority Research Program of Chinese Academy of Sciences (Grant No. XDB28000000), the Fundamental Research Funds for the Central Universities, and the Research Funds of Renmin University of China.

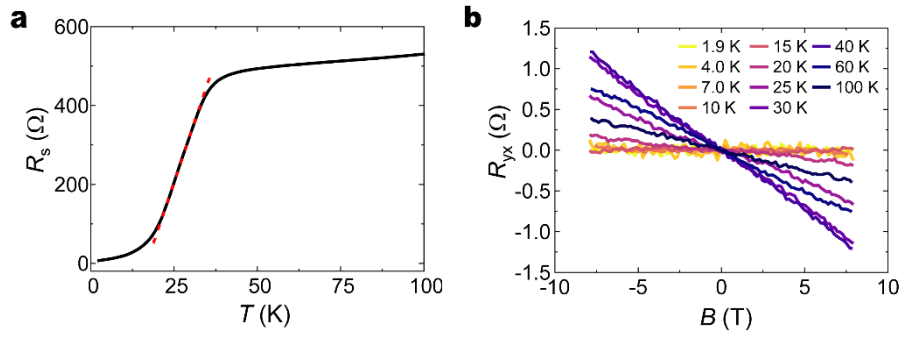
Author contributions J.W. conceived and supervised the project. Y.N.L., Y.L., S.C.Q., H.R.J., C.C.J. and Z.H.C. analyzed the data under the guidance of J.W.. J.W., Y.N.L., Y.L., Y.S., S.C.Q. and H.R.J. performed the transport measurements. H.W.L. and X.C.X. carried out theoretical work. W.F.D., W.H.Z., L.L.W. and Q.-K.X. grew the films. Y.N.L., H.R.J. and S.C.Q. fabricated the JJA samples. Y.N.L., Y.L. and J.W. wrote the manuscript with the input from H.W.L., S.C.Q., H.R.J. and N.S.. All authors contributed the related discussions.

Competing interests The authors declare no competing interests.

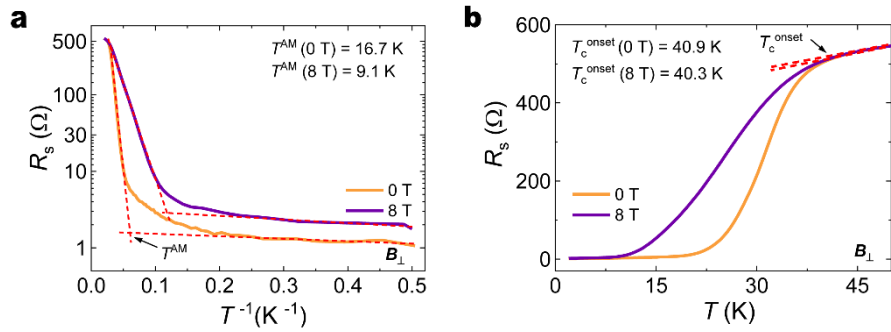
Data availability Data measured or analyzed during this study are available from the corresponding author on reasonable request.



Extended Data Fig. 1| Typical STM topography of FeSe films on SrTiO₃ (001) substrates showing the lattice structure. The sample bias $V_s=80$ mV and the tunneling current $I_t=2.1$ nA. The image is 5.6×5.6 nm².

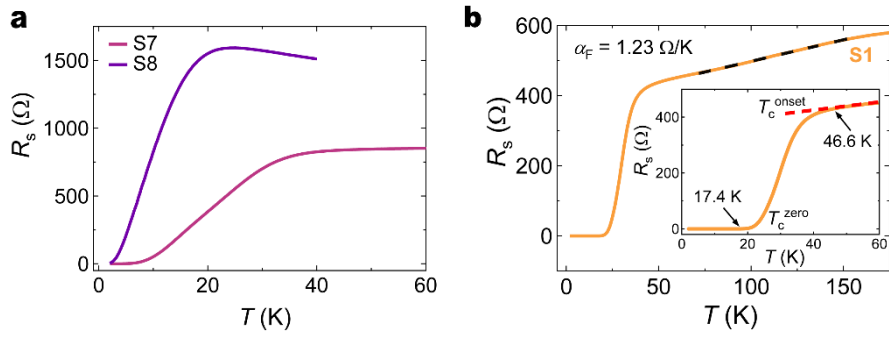


Extended Data Fig. 2 | $R_s(T)$ curve (a) and Hall resistance under perpendicular magnetic fields (b) of FeSe/SrTiO₃ (S3 in Fig. 1a, b). The Hall resistance decreases to zero within the measurement resolution below 20 K.

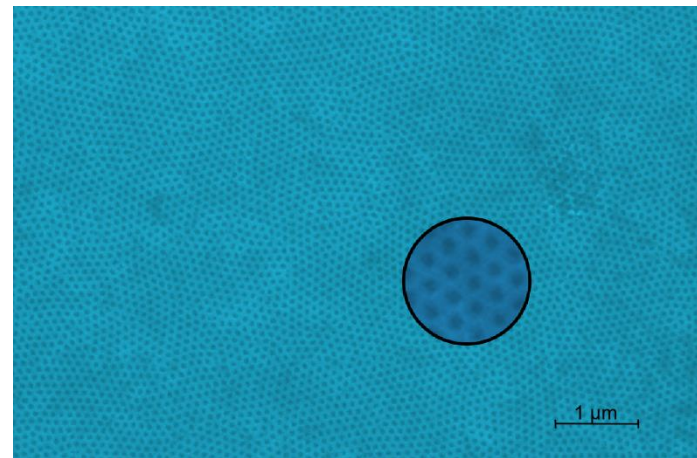


Extended Data Fig. 3 | High-temperature anomalous metal state in FeSe/SrTiO₃.

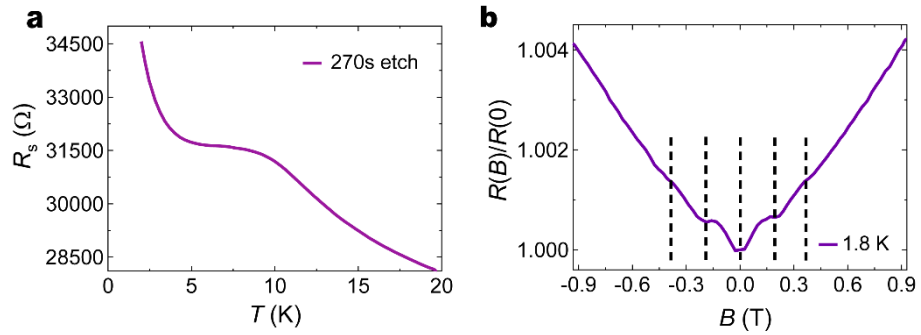
a, Arrhenius plot of $R_s(T)$ curves under perpendicular fields (S2 in Fig. 1a). T^{AM} is the temperature of the crossing point of the slanted and the horizontal lines. **b**, Linear plot of $R_s(T)$ curves in **a**. T_c^{onset} is defined as the temperature when the sheet resistance begins to deviate from the linear extrapolation of the normal state.



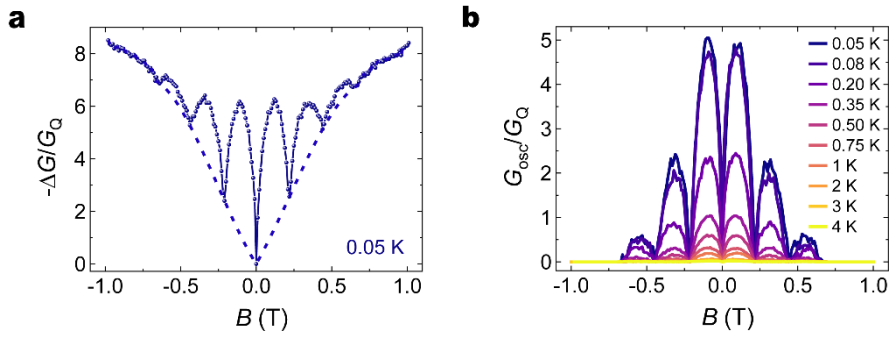
Extended Data Fig. 4 | Electric transport behavior of FeSe/SrTiO₃ at zero field. **a**, Temperature dependence of sheet resistance R_s of FeSe/SrTiO₃ with T -linear resistance below T_c^{onset} . The resistance either show insulating behavior or barely change above T_c^{onset} . **b**, Temperature dependence of sheet resistance $R_s(T)$ of superconducting FeSe/SrTiO₃ (S1 in Fig. 1a). The dashed line is the linear fitting of the $R_s(T)$ curve above T_c^{onset} , yielding the slope $\alpha_F = 1.23 \Omega/\text{K}$.



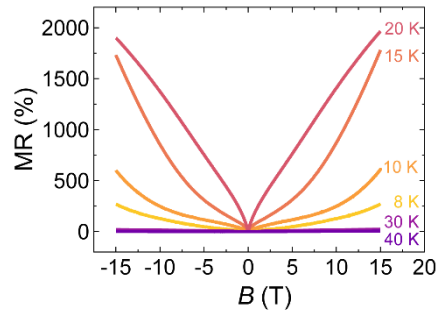
Extended Data Fig. 5 | Typical scanning electron microscope image of a nanopatterned FeSe film. The inset is the zoom-in of the nanopatterned structure.



Extended Data Fig. 6 | Insulating state of nanopatterned FeSe/SrTiO₃ (270 s etched film). **a**, $R_s(T)$ curve of 270 s etched FeSe film, showing an insulating state. **b**, Magnetoresistance of 270 s etched FeSe film at 1.8 K. Magnetoresistance oscillations with period ~ 0.215 T are observed, corresponding to one superconducting flux quantum per unit cell of the nanopattern, which indicates the bosonic nature of the insulating state.



Extended Data Fig. 7 | Background subtraction of magnetoconductance oscillations of 210 s etched film. **a**, Negative change of magnetoconductance $-\Delta G/G_Q$ at 0.05 K. $-\Delta G = G_0 - G(B)$, where G_0 is the conductance at zero magnetic field. The dashed line is the polynomial fitting of the magnetoconductance background. **b**, Magnetoconductance oscillations at various temperatures. G_{osc} is the amplitude of conductance after subtracting the background.



Extended Data Fig. 8| Magnetoresistance comparison between the high-temperature anomalous metal state and normal state of FeSe/STO (S6 in Fig. 1c, d). The magnetoresistance ($MR = (R(B) - R(0))/R(0) \times 100\%$) is 270%-1900% below T_{AM} (20 K) at 15 T. Above $T_{\text{c}}^{\text{onset}}$, the magnetoresistance is only 3.5% at 40 K and 15 T.

Extended Data Table 1 | Parameter n of the power law fitting of $R_s(T)$ with ($R_s(T) = a + bT^n$) of bosonic strange metal states.

S7 (Fig. 2a)		B_{\perp}	0 T	0.5 T	2 T	8 T	16 T
		n	0.976 ± 0.002	1.046 ± 0.002	1.059 ± 0.002	1.006 ± 0.003	0.976 ± 0.003
		T_2 (K) – T_1 (K)	26.9 – 3.3	26.5 – 11.7	26.3 – 11.1	24.3 – 9.2	21.9 – 8.5
S8 (Fig. 2d)		B_{\perp}	0 T	1 T	5 T	10 T	15 T
		n	0.972 ± 0.014	0.964 ± 0.004	0.884 ± 0.087	0.853 ± 0.010	0.989 ± 0.079
		T_2 (K) – T_1 (K)	11.9 – 3.6	11.6 – 2.0	10.5 – 2.0	5.6 – 2.1	3.9 – 2.0
S8 (Fig. 2g)		B_{\parallel}	0 T	1 T	5 T	10 T	15 T
		n	1.010 ± 0.013	1.012 ± 0.066	1.014 ± 0.008	0.944 ± 0.039	0.897 ± 0.004
		T_2 (K) – T_1 (K)	12.4 – 3.7	13.2 – 3.7	13.1 – 2.0	12.3 – 2.0	8.3 – 2.1
Fig. 3		etching time	210 s	150 s	90 s	0 s	
		n	0.989 ± 0.053	0.993 ± 0.017	1.141 ± 0.032	0.992 ± 0.012	
		T_2 (K) – T_1 (K)	8.7 – 1.0	8.7 – 1.8	9.0 – 6.2	9.2 – 7.2	

T_2 and T_1 are the upper and lower boundaries of the temperature range for power law fitting of the $R_s(T)$. ΔT in Fig. 2 and Fig. 3 equal T_2 - T_1 . T_c^{onset} for S7 (0 T), S8 (0 T) and 0 s etched film in Fig. 3 are 48.1 K, 24.7 K and 12.4 K, respectively. n is around 1, indicating the T -linear resistance. For sample S7 and S8, the temperature range of linear $R_s(T)$ is larger at low fields but smaller at high fields. For etched samples, the longer etching time yields a wider temperature range of linear $R_s(T)$ curves.